

## **CHAPTER - 3**

### **Breakup threshold anomaly in the near-barrier elastic scattering of ${}^6\text{Li} + {}^{116,112}\text{Sn}$**

<b>3.1</b>	<b>Introduction</b>	<b>46</b>
<b>3.2</b>	<b>Experimental Description</b>	<b>48</b>
	<b>3.2.1 The Pelletron Accelerator Facility</b>	<b>48</b>
	<b>3.2.2 Energy Loss Calculations</b>	<b>53</b>
	<b>3.2.3 Detection techniques</b>	<b>53</b>
	<b>3.2.3.1 Semiconductor Detectors</b>	<b>55</b>
	<b>3.2.3.2 Silicon surface barrier detector</b>	<b>57</b>
<b>3.3</b>	<b>Experiment Details</b>	<b>58</b>
<b>3.4</b>	<b>Electronics and Data acquisition</b>	<b>61</b>
<b>3.5</b>	<b>Optical model analysis of the elastic scattering</b>	<b>62</b>
	<b>3.5.1 Analysis Using Phenomenological Woods-Saxon Potential</b>	<b>62</b>
	<b>3.5.2 Analysis Using the Double-Folding São Paulo Potential</b>	<b>70</b>
<b>3.6</b>	<b>Total reaction cross sections for different systems</b>	<b>72</b>
<b>3.7</b>	<b>Effects of breakup couplings on the <math>{}^6\text{Li} + {}^{116}\text{Sn}</math></b>	<b>76</b>
<b>3.8</b>	<b>Conclusions</b>	<b>81</b>
	<b>References</b>	<b>82</b>

#### **Published in:**

1. **N. N. Deshmukh** *et al.*, *Breakup threshold anomaly in the near barrier elastic scattering of  ${}^6\text{Li} + {}^{116,112}\text{Sn}$* , Phys. Rev. C **83**, 024607 (2011).
2. **N. N. Deshmukh** *et al.*, *Effect of breakup couplings on the  ${}^6\text{Li} + {}^{116}\text{Sn}$  elastic scattering*, Physical Review C (2012) – Communicated.

### 3.1 Introduction

It is a well established fact that the near barrier elastic scattering of tightly bound heavy ions show up a behavior of the energy dependence of the interacting optical potential (OP) known as Threshold Anomaly (TA) [1 - 3]. The basic characterization of the above terminology is the observation of a localized peak in the real part of the potential accompanying the sharp decrease of the imaginary part of the potential as the bombarding energy declines towards the Coulomb barrier. The name “anomaly” comes from the expectation that the real and imaginary parts of the OP are energy independent at higher energies, but not at near barrier energies. The TA has been understood in the sense that an attractive polarization potential  $\Delta V$  arises from the coupling of elastic scattering to the other reaction channels at low energies, leading to a real potential  $V_{\text{eff}} = V_0 + \Delta V$ , where  $V_0$  is the real potential at higher energies. In brief, the coupling to the channels other than elastic introduces an attractive real potential and the result of the decrease of the imaginary potential is tacit by the closure of the nonelastic channels at energies near and below the Coulomb barrier. It has been shown [4, 5] that there is a connection between the real and imaginary parts of the OP due to causality and subsequently they obey the dispersion relation. The attractive polarization potential has the effect of enhancing the fusion cross section, since it decreases the Coulomb barrier.

This situation may change in the scattering of weakly bound nuclei [6]. These nuclei have very low breakup threshold energies and so, have a large breakup (BU) probability. At energies above the barrier, fusion cross sections are usually larger than BU cross sections, but at energies close to the barrier, the opposite occurs, and furthermore, BU probabilities remain large even at energies below the Coulomb barrier [7 - 16]. The BU process feeds states in the continuum and produces a repulsive polarization potential [17 - 25]. This fact is compatible with the recently demonstrated [26 - 28] systematic suppression of fusion cross section of weakly bound systems at near barrier energies, due to dynamic effects of BU.

Therefore, the net polarization potential in the scattering of weakly bound nuclei has two components: one attractive, due to the couplings of the elastic channel with inelastic excitations and other direct reactions and one repulsive, due to the BU. The relative importance of each

component determines the final behavior of the polarization potential: if the attractive potential predominates, the usual TA may still be observed. Otherwise, an “anomalous behavior” will be observed for such systems, where, ironically, the new “anomaly” will be the absence of the TA. In such situation one says that the system presents the Breakup Threshold Anomaly (BTA) [29, 30]. So, contrary to what is written in some papers in the literature, BTA is the absence of TA at the Coulomb barrier, and not necessarily the rise of the imaginary potential when the bombarding energy decreases towards the barrier. Since the BU cross section does not decrease significantly in the vicinity of the Coulomb barrier, this is no longer the threshold of the closing of the reaction channels. When the repulsive BU polarization predominates, BTA is more clearly observed by the increasing of the imaginary potential as the energy decreases, associated with a small reduction in the real part of the potential near the barrier. In any situation, the real and imaginary parts of the OP should satisfy the dispersion relation.

Although several works have been reported on the elastic scattering of weakly bound nuclei, both stable [13 - 15, 17, 18, 29 - 48] and radioactive [49, 50, 51], a systematic behavior of the energy dependence of the OP for such systems has not yet been reached. One of the reasons is that the net polarization potential, composed by competing attractive and repulsive parts, depends strongly on the properties of the weakly bound projectiles, such as their BU energy threshold and the presence of bound inelastic states. The target structure also plays an important role, since it may produce strong attractive polarization potential and the relative importance of the Coulomb breakup depends on the target mass. Another reason is concerned with the difficulties of the measurements, since one needs very precise data in a large range of the scattering angle and at low energies, where the scattering is almost entirely of the Rutherford type, and therefore, it is difficult to extract the interaction potential from the data. One example of this last difficulty is the fact that, among several works in this field, only very recently [41] it was possible to estimate, from experimental data extrapolation, the energy below the Coulomb barrier for which the imaginary potential vanishes.

In the present work we try to contribute to this field by investigating the elastic scattering of the  ${}^6\text{Li} + {}^{116,112}\text{Sn}$  systems through very precise and complete angular distributions at energies from below the Coulomb barrier to approximately twice this value. The  ${}^6\text{Li}$  projectile has break-

up ( $\alpha + d$ ) threshold energy of 1.48 MeV and no bound excited state. We also derive the total reaction cross section for these systems and compare them with cross sections for other weakly and tightly bound systems with targets in the same mass region, in order to investigate the role of BU on the total reaction cross section. Apart from this, the effect of the breakup channel on the elastic angular distributions for  ${}^6\text{Li} + {}^{116}\text{Sn}$  system using the CDCC method was also studied.

## 3.2 Experimental Description

Particle accelerator, devices that accelerates a beam of fast-moving, electrically charged atoms (ions) or subatomic particles are used to study the structure of atomic nuclei and the nature of subatomic particles and their fundamental interactions. At speeds close to that of light, particles collide with and disrupt atomic nuclei and subatomic particles, allowing physicists to study nuclear components and to make new kinds of subatomic particles. In India, several accelerators have been established to pursue research in nuclear, atomic, condensed matter physics and interdisciplinary areas. The present thesis reports the experimental investigation on reaction mechanism carried out using 14 UD Pelletron Accelerator set up as a collaborative project between the Bhabha Atomic Research Centre (BARC) and the Tata Institute of Fundamental Research (TIFR). This has been serving as a major facility for heavy ion accelerator based research in India since its commissioning in December 1988. The concise description of accelerator facility is described below.

### 3.2.1. The Pelletron Accelerator Facility

The Pelletron Accelerator [52] was installed in December 1988 and experiments using the beam were started in the middle of 1989. The schematic diagram of the 14 UD BARC – TIFR pelletron accelerator facility, Mumbai [53] is shown in the Fig. 3.1. The source for the charged particles is located at the top of the accelerator tower. A Cesium sputter ion source generates negative ions, which are initially accelerated to low energies (150-250 keV) in a short horizontal section. These low energy negative ions are then bent through  $90^\circ$  using an injector magnet into the vertical accelerating column. In the initial stage, the acceleration results from the

electrostatic attraction of the negative ions by the positively charged high voltage terminal situated in the middle of the column. The high electric potential at the terminal is achieved by a continuous transfer of charge to the terminal by means of the chain of steel pellets and hence the name *Pelletron* accelerator. Thus negative ions gain energy of  $V_T$  MeV, where  $V_T$  is the terminal voltage in MV (million volts). Thus for the present accelerator the maximum achievable terminal voltage is 14 MV. This method leads to more uniform charging compared to moving charging belt and hence less ripple on the HV terminal. Inside the terminal the ions pass through a thin carbon foil ( $\sim 5 \mu\text{g}/\text{cm}^2$ ) or a small volume of a gas, where they lose electrons and acquire a high positive charge. The average charge of the ion depends upon the type of ion and the terminal voltage. Now the positive voltage of the terminal acts repulsively on the positive ions when they enter in the second or high energy stage of acceleration. This results in the energy gain of  $qV_T$  MeV for an ion with charge  $q$ . Thus the total energy gain of the ion becomes

$$E = (q + 1) \times V_T \text{ MeV} \quad (3.1)$$

For example, the final energy at the maximum terminal voltage for our case  ${}^6\text{Li}^{+3}$  is 56 MeV, where the maximum charge stripped will be  $q = 3$  and  $V_T = 14$  MV. Thus the beams ranging from protons to uranium are accelerated in the existing accelerator. An analyzing magnet is placed at the end of the accelerating tube, which serves the purpose of charge and energy selection of the ion. The energy of the analyzed ions of mass number  $A$  and charge state  $q$  in this accelerator is given by the relation [54]

$$B = 720.76 \frac{\sqrt{AE}}{q} \quad (3.2)$$

where  $B$  is the magnetic field in the Gauss and  $E$  is the energy in MeV. This analyzed beam of ions is then transported to the experimental setup with the help of switching magnet.

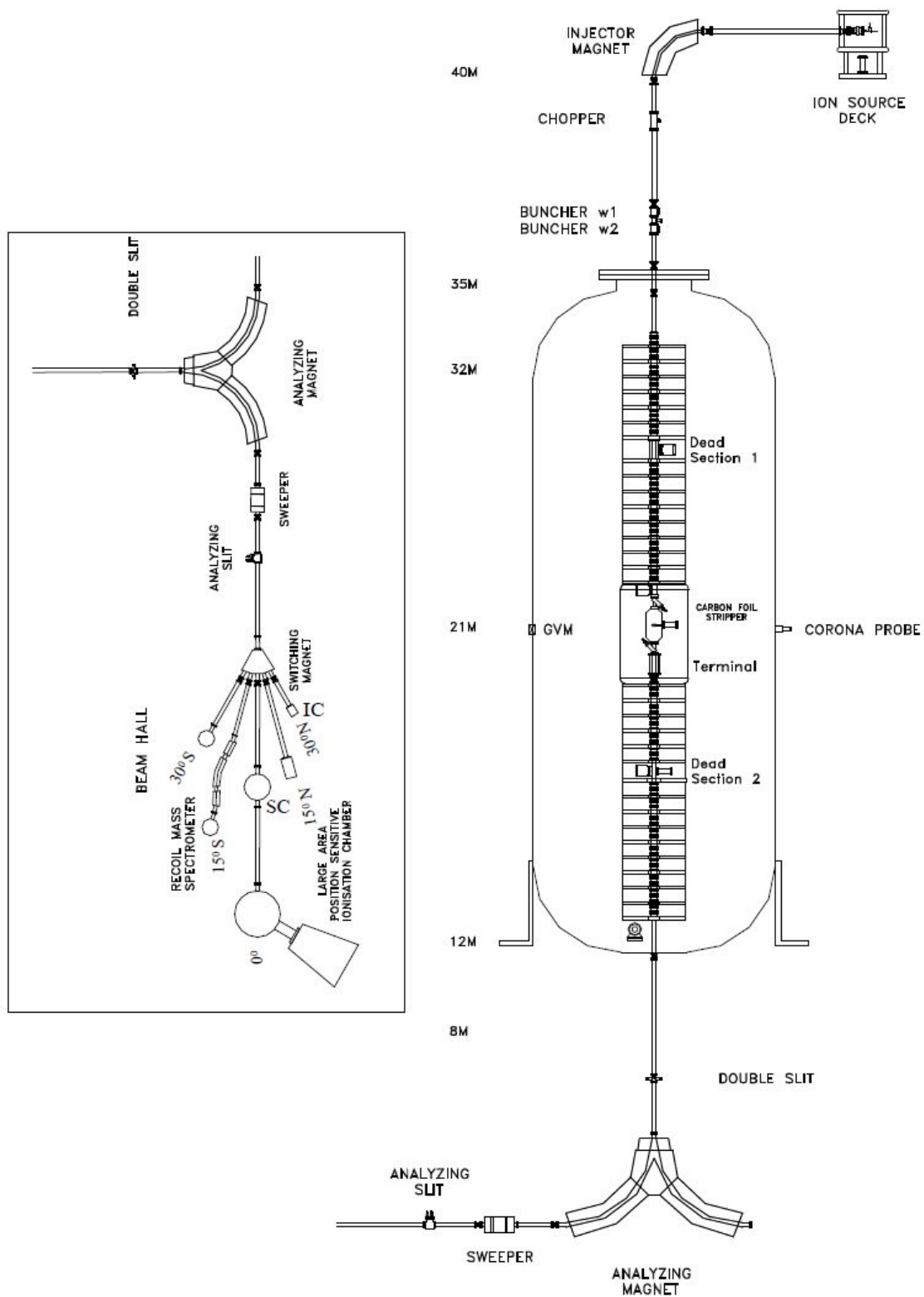


**Figure 3.1 Schematic diagram of the Pelletron accelerator facility, Mumbai. The left panel of the figure shows the 5 beam lines.**

There are five beam lines in the accelerator facility. The beam transport system on these lines is remotely controlled using a CAMAC system and integrated with the indigenously developed PC based control system of the main accelerator [55]. These beam lines are as listed below:-

1. The 30° North is essentially use for irradiation of nuclear targets and other samples for radiochemical, material and biological studies. It is also used for the AMS measurements.
2. The 15° North is mainly used for gamma – ray, neutron and charge particle spectra measurements.
3. The 0° is connected with the general purpose scattering chamber (GPSC) which usually facilitates to measure the cross sections and angular distributions for various nuclear reactions by mounting the various detectors, telescopes etc. This beam line is further extended to house one small scattering chamber with large area position sensitive deep ionization chamber meant for fission studies.
4. The 15° South is set aside for recoil mass separator.
5. The 30° South is intended for gamma – ray, charge particle and atomic physics measurements.

A photograph of the five beam lines is shown in the next page (Fig. 3.2) with best possible view of the all above mentioned beam lines. Moreover the measurements using the weakly bound nuclei in this thesis were carried out in 0° beam line using the general purpose scattering chamber.

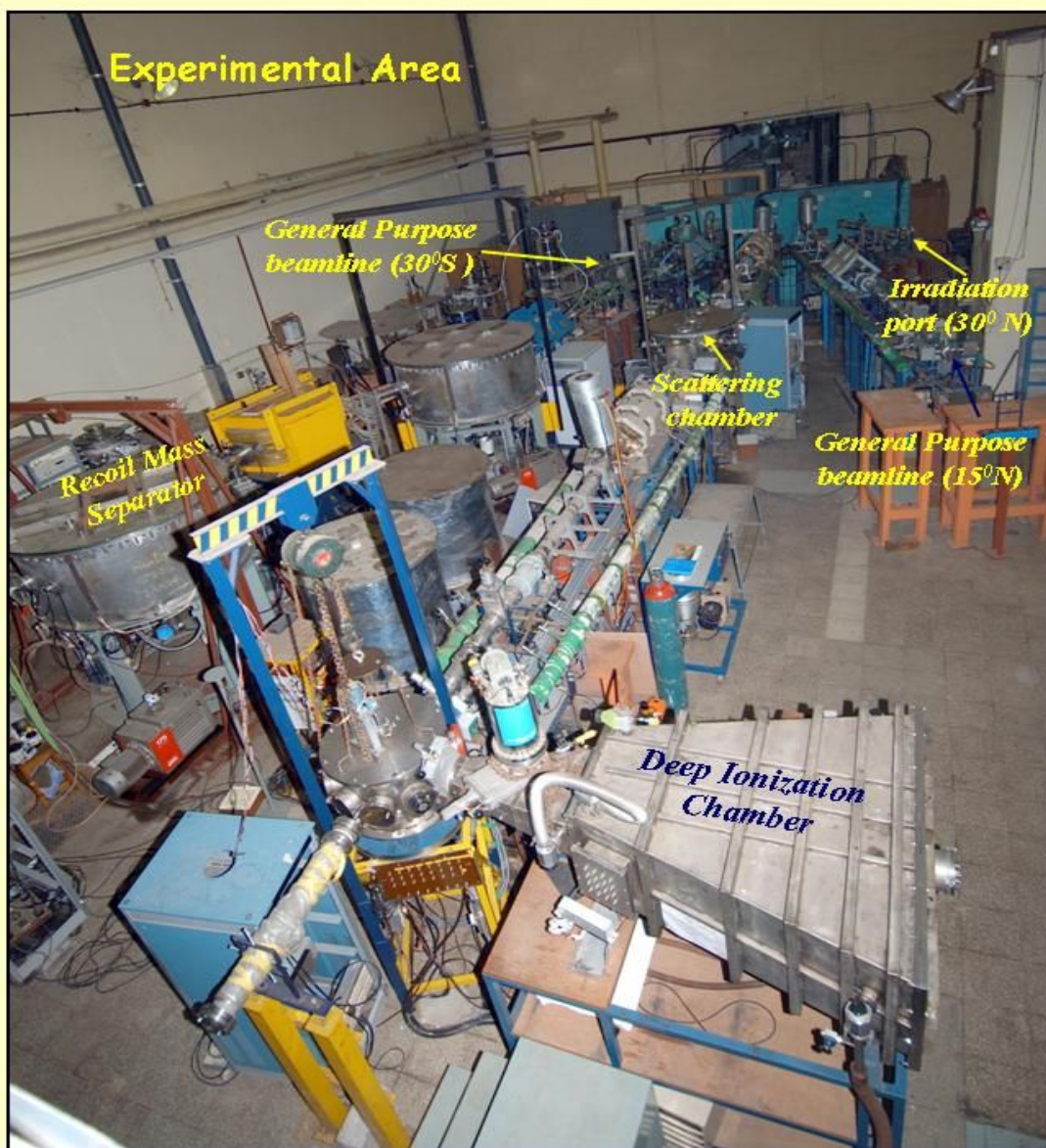


Figure 3.2 Photograph of the experimental area at TIFR where the all five beam lines are located.

### 3.2.2. Energy Loss Calculations

When an energetic beam interacts with the target there is momentary electrostatic interaction between it and the atoms of the target by which it is passing. As a result of which it loses some energy in continuation with the elastic fragments, which loses partial or full energy in the  $\Delta E$  detector. This energy loss is also of prime importance for the kinematical calculations and data analysis. The energy loss for the  ${}^6\text{Li}$  in the targets and elastic fragments in the  $\Delta E$  detector were calculated by using the program stopping power and range of ions in matter (SRIM) [56]. The amount of energy lost ( $\Delta E$ ) is inversely proportional to the beam energy and is given by the relation,

$$\frac{dE}{dx} \propto \frac{MZ^2}{E} \quad (3.3)$$

The respective energy loss of the  ${}^6\text{Li}$  beam in  $450 \mu\text{g}/\text{cm}^2$   ${}^{116}\text{Sn}$  &  $540 \mu\text{g}/\text{cm}^2$   ${}^{112}\text{Sn}$  targets was 77 KeV and 94 KeV.

### 3.2.3. Detection techniques

The past few years have seen a rapid development of techniques by which the identity of species produced in nuclear reactions may be established. Writing a nuclear reaction in the usual way –  $X(a, b)Y$  – we review methods for the identification of  $b$  by determining its atomic number  $Z$  and mass number  $A$ . Generally the energy  $E$  of the particle must also be measured, and with the best possible resolution. It is sufficient, in many experiments, to measure the kinetic energy differences between more or less sharp lines in the energy spectrum of particle  $b$ , corresponding to the formation of discrete energy states of the residual nucleus  $Y$ . If the energies of the states of  $Y$  are well known from previous work, the energy differences need only be measured with sufficient precision to be sure that lines in the  $b$  spectrum are correctly associated with states of  $Y$ . Nuclear energy levels, however, are often closely spaced so only a small spread in the  $E$  measurement can be tolerated even though an absolute determination of  $E$  may not be important.

A complete determination of  $Z$ ,  $A$ , and  $E$  requires the measurement of three quantities that are independent functions of  $Z$ ,  $A$ , and  $E$ . No measurable quantities depend directly upon  $A$ , but for the non- or only slightly relativistic particles typically encountered in nuclear physics experiments,  $A$  is very nearly equal to the mass  $M$  of the particle (in atomic mass units), which is measurable. For non – relativistic particles,  $M$  has only near-integral values.  $M$  and  $Z$  therefore need be determined only with enough accuracy to separate them from adjacent integral values. This is very easy for light particles (e.g. H and He isotopes) because the fractional differences between adjacent small integers are large. For heavy particles, the necessary resolution becomes difficult or even impossible to achieve. Several types of measurements depend on independent functional combinations of  $M$ ,  $Z$ , and  $E$ , but no one measurement uniquely determines these parameters. The value of  $E$  is nearly always required in an experiment but, fortunately, individual values of  $M$  and  $Z$  are often not needed. For example, the quantity  $MZ^2$  can be obtained from a detector telescope that measures the energy loss of a particle passing through a thin detector into a second detector where its residual energy is deposited and measured.  $MZ^2$  assumes unique values of 1, 2, 3, 12, and 16 for protons, deuterons, tritons,  $^3\text{He}$ , and  $^4\text{He}$ , respectively, so its value characterizes each of these isotopes unambiguously. For heavier ions more elaborate identification measurements are needed to discriminate between different ions. The following is a brief summary of the various methods and the information they yield:

(a) Total absorption in a detector (or detector telescope): Measurement of the total ionization produced in the detector(s) provides a linear measure of the particle energy  $E$ .

(b) Energy absorption in a thin detector: A thin transmission detector, included in the detector telescope, provides a direct measurement of  $dE/dx$  for a particular segment of a particle's track. The rate of energy loss is approximately given by the simplified Bethe – Bloch [57] equation:

$$-dE/dx = (aZ^2c^2/v^2) \ln [bv^2/(c^2 - v^2)], \quad (3.4)$$

where  $v$  is the particle velocity,  $c$  is the velocity of light and  $a$  and  $b$  are constants dependent only on the detector material. Although this equation is traditionally written in terms of the atomic number  $Z$ , the rate of energy loss actually depends on the rms charge state  $q_{\text{eff}}$  of the moving ion,

which may not be fully stripped of atomic electrons (i.e.  $q_{\text{eff}} \leq Z$ ). Since the logarithmic term varies only slowly with energy (or velocity) its effect will be neglected in this brief discussion. Also for the non – relativistic particles,  $v^2 = 2E/M$ . Therefore equation (3.4) can be simplified to equation (3.3), where E can be computed by summing the detector telescope signals, so the measurement of  $dE/dx$  provides a measure of  $MZ^2$ .

(c) Time-of-flight measurement: Measurement of the time of flight (TOF) of a particle through a known flight path in vacuum determines the particle velocity  $v$ . We have

$$v^2 = 2E/M \quad (3.5)$$

If the value of E is known, then the TOF determines M. If this measurement of M is combined with a  $dE/dx$  determination, Z (or more accurately  $q_{\text{eff}}$ ) can be determined.

(d) Bending in a magnetic field: Magnetic spectrometers provide yet another determination of a combination of the particle parameters M, Z, and E. In a fixed magnetic field B, the radius of curvature  $\rho$  of a particle is given by

$$B\rho \propto Mv/q \quad (3.6)$$

where q is the average charge of the ion. Since light particles, or heavy ions at high energies, emerge from a target fully stripped of electrons, their average charge q is equal to Z, and measurement of  $B\rho$ , TOF, and  $dE/dx$  is equivalent to a complete identification and energy measurement. For heavy ions at lower energies,  $q \leq Z$  and there may be ambiguities in the identifications. Other physical effects that depend on M, Z, and E can also, in principle, be used for particle identification. The deflection of a particle in an electric field is one example, but it is so small for high-velocity particles that its use is not very practical.

In the present study,  $\Delta E - E$  surface barrier detector telescopes have been used for the detection of the light charged particles produced in the reactions.

### 3.2.3.1 Semiconductor Detectors

The material having an electrical conductivity between a conductor and an insulator is known as a semiconductor. Crystals of semiconductor materials like silicon and germanium are

suitable for radiation detection. The energy gap between the electrons in the valence band (electrons that are part of the covalent bond in the crystal) and the electrons in the conduction band (electrons responsible for electrical conductivity) is only about 1 eV compared to 5-6 eV for the inorganic scintillation detection. As in the case of gas filled detectors, radiation detection depends on the creation of charge carriers by the interaction of radiation with the detector, and their collection. Electrons in the valence band are lifted to the conduction band by the energy imparted by radiation, and a corresponding hole is left in the valence band. Since the band gap is small (0.67 eV for Ge and 1.12 eV for Si) the number of charge carriers per unit of energy absorbed is large. As against 100-200 eV required for getting one electron in an inorganic scintillators, or 35 eV required for producing an ion pair in gas detectors, producing an electron-hole pair requires 2.96 eV in Ge and 3.76 eV in Si. This reflects in good energy resolution in these detectors.

The small band gap is useful in producing a large number of charge carriers but there are some drawbacks related to this. Thermal excitation can lift the electrons in the valence band to the conduction band. In a completely pure semiconductor the number of electrons in the conduction band is equal to the number of holes in the valence band. For example the intrinsic hole concentration in the valence band (or electron concentration in conduction band), at room temperature, is  $1.5 \times 10^{10} \text{ cm}^{-3}$  in silicon and  $2.4 \times 10^{13} \text{ cm}^{-3}$  for germanium. However, it is virtually impossible to get crystals with no impurities and very small levels of residual impurities dictate the electrical properties of real materials. For example, presence of 2 parts per million ( $10^{17}$  atoms  $\text{cm}^{-3}$ ) of phosphorous (pentavalent) in silicon (tetravalent) would add  $10^{17}$  non-bonded electrons per  $\text{cm}^{-3}$  in the material. These electrons can move to the conduction band leaving ionized phosphorus item at silicon lattice sites. This increase in the concentration of electrons in the conduction band leads to a decrease in the concentration of holes in the valence band, since the product of electron and hole density should be the same for impure and intrinsic material. So the hole concentration in silicon with phosphorus impurity would decrease to  $2 \times 10^3 \text{ cm}^{-3}$ . In fact doping with phosphorus is used to prepare n-type semiconductors in which the majority of the charge carriers are electrons. Similarly silicon can be doped with a trivalent element (e.g. boron) to get p-type semiconductors in which a majority of charge carriers are holes. Heavily doped

materials, called  $n^+$  type and  $p^+$  type, have good electrical conductivity and are useful for making electrical contacts.

When a p-type material is brought in contact with an n-type material, electrons from n-type diffuse across the junction and holes from p-type also diffuse across junction resulting in the formation of a depletion region. If a reverse bias is applied across the junction (+ve on n-type and -ve on p-type side), providing a field of the order of  $10^3 \text{ Vcm}^{-1}$ , the depth of the depletion region is increased. This results in extremely low leakage current and useful for radiation detection. This depletion region is the active volume of a detector. Electron-hole pairs produced in the depletion region due to interaction of radiation will be swept out of the depletion region by the applied electric field and their motion constitutes the basic signal for radiation measurement.

### **3.2.3.2 Silicon surface barrier detector**

In our set of experiments the semiconductor detector used was the silicon surface barrier detector. A silicon surface barrier detector has been widely used for charged particle detection. It consists of an extremely thin p-type layer produced on a high purity n-type silicon wafer, thus forming a large area p-n junction diode. A n-type silicon wafer is taken and one of its faces is etched with an acid, most likely, CP4A ( $\text{HNO}_3 + \text{HF} + \text{CH}_3\text{COOH}$  in the ratio 5:3:3) and are mounted on ceramic or teflon mounts exposing it to air. An oxidation layer is formed on the etched surface and this layer acts like a very thin p-type layer. Electrical contacts are provided by evaporating thin gold film on the p-type surface and thin aluminium film on the back surface of n-type silicon layer. The noteworthy characteristics of the surface barrier detectors are as follows:

- (a) Linear energy response at different energies for different types of particles.
- (b) High energy resolution which gives rise to narrow pulses.
- (c) Time response is very quick because of the short distance moved by the electron-hole pairs before collection.
- (d) Differential sensitivity, because of the inability of the detectors to detect neutrons and photons, which makes possible charged particle detection against the background of these radiations.

- (e) High conversion efficiency, due to the much smaller energy required for producing electron-hole pairs ( $\sim 3$  eV) which is less than one-tenth of that required in the case of gaseous ionization detectors. This results in the larger number of electron-hole pairs.

Thus in our set of experiments we used this silicon surface barrier detectors as both  $\Delta E$  and E detectors.

### 3.3 Experiment Details

The experiment was performed at Bhabha Atomic Research Centre - Tata Institute of Fundamental Research (BARC-TIFR) pelletron facility, Mumbai, India. The beam of  ${}^6\text{Li}^{+3}$  was delivered by the 14UD Pelletron accelerator covering the energy range from below to twice the Coulomb barrier (the nominal barrier is around 22.4 MeV): 20, 21, 22, 23, 26, 30 and 35 MeV for the  ${}^6\text{Li} + {}^{116}\text{Sn}$  system, and 21, 23, 25, and 35 MeV for the  ${}^6\text{Li} + {}^{112}\text{Sn}$  system. Beam currents were ranging between 2.5 - 30 nA. The beam energies were corrected for the half target thickness in the analysis process that amounts to a maximum of 92 keV for 20 MeV and a minimum of 63 keV for 35 MeV for  ${}^6\text{Li} + {}^{116}\text{Sn}$  system and a maximum of 110 keV for 21 MeV and a minimum of 79 keV for 35 MeV for  ${}^6\text{Li} + {}^{112}\text{Sn}$  system. The beam bombarded consecutively a  $450 \mu\text{g}/\text{cm}^2$  and a  $540 \mu\text{g}/\text{cm}^2$ , self supported enriched  ${}^{116,112}\text{Sn}$  ( $\geq 98\%$  and  $99.5\%$ ) targets, respectively, and the elastically scattered  ${}^6\text{Li}$  ions were detected by three solid state silicon surface barrier detectors in  $\Delta E + E$  telescopic arrangements. The telescopes used had thickness ( $T_1$ ) with  $\Delta E = 30 \mu\text{m}$  and  $E = 300 \mu\text{m}$ , ( $T_2$ ) with  $\Delta E = 25 \mu\text{m}$  and  $E = 1 \text{ mm}$ , and ( $T_3$ ) with  $\Delta E = 50 \mu\text{m}$  and  $E = 2 \text{ mm}$ . Two monitor detectors with thickness  $M_1 = 200 \mu\text{m}$  and  $M_2 = 600 \mu\text{m}$  were used for absolute normalization and beam monitoring. The telescopes were placed on a rotating arm inside a 1 meter scattering chamber at angular separation of  $10^\circ$  between consecutive telescopes and the monitors were placed at  $\pm 20^\circ$ . The angular distributions were measured in steps of  $2.5^\circ$  to  $5^\circ$  at angles from  $20^\circ$  to  $173^\circ$  at lower energies and from  $20^\circ$  to  $105^\circ$  for higher energies. The experimental set up used for the elastic scattering angular distribution measurements is as shown in Fig. 3.3 (a), (b).

To obtain the relative solid angle, data were also taken at overlapping angles in the telescopes detectors. The measured statistical error in the data was less than 1% in the forward angles and maximum 2% at the backward angles. Figure 1a shows a typical bi-parametric E- $\Delta$ E spectrum for the  ${}^6\text{Li} + {}^{116}\text{Sn}$  system at  $E_{\text{Lab}} = 35 \text{ MeV}$  and  $\theta = 35^\circ$ . The inset of Fig. 3.4 shows the corresponding projection for the  $Z = 3$  events.

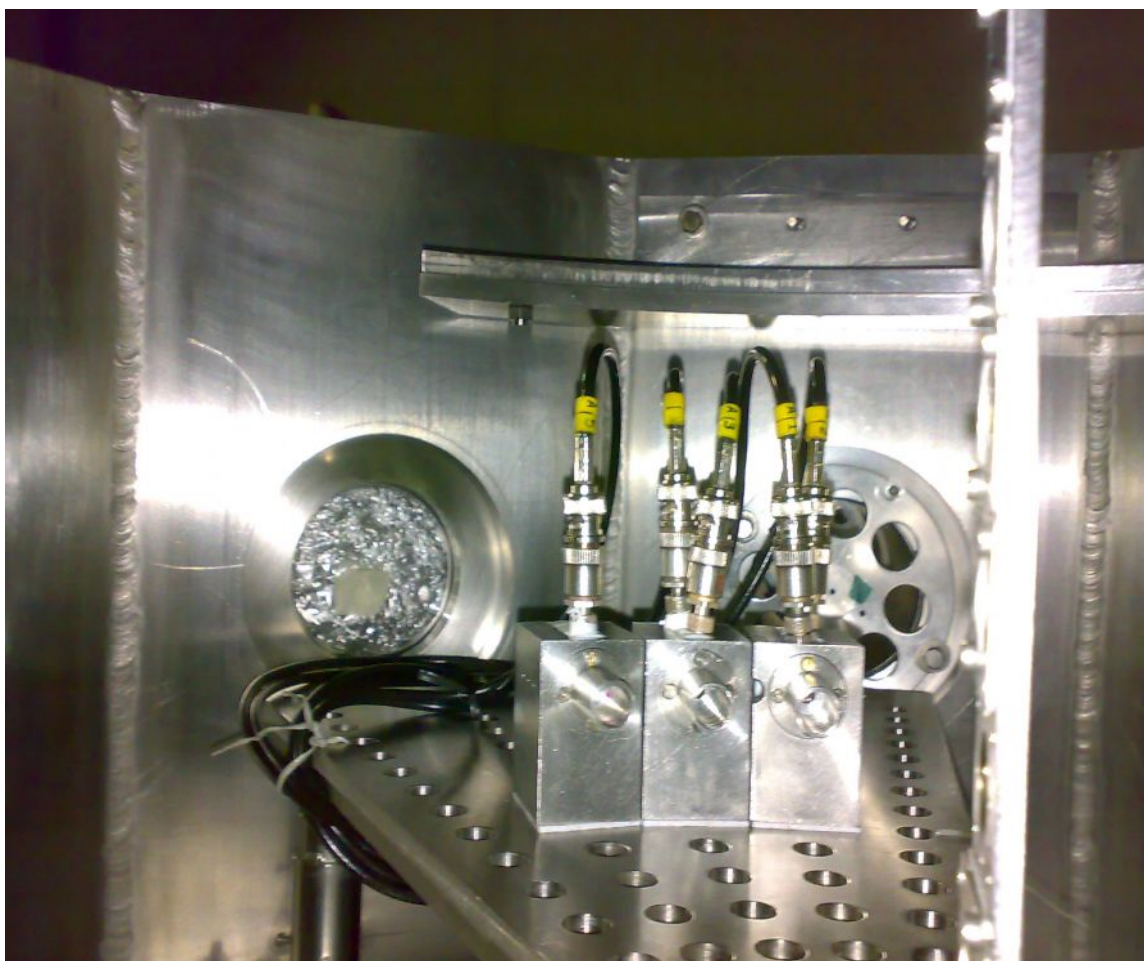


**Figure 3.3 (a) Three solid state silicon surface barrier detectors placed on the one arm (movable) of the scattering chamber. The target mounted in a target ladder is also shown in the picture.**



**Figure 3.3 (b) Two monitor detectors for absolute normalization were kept hanging (fixed) in the scattering chamber at  $\pm 20^\circ$ .**

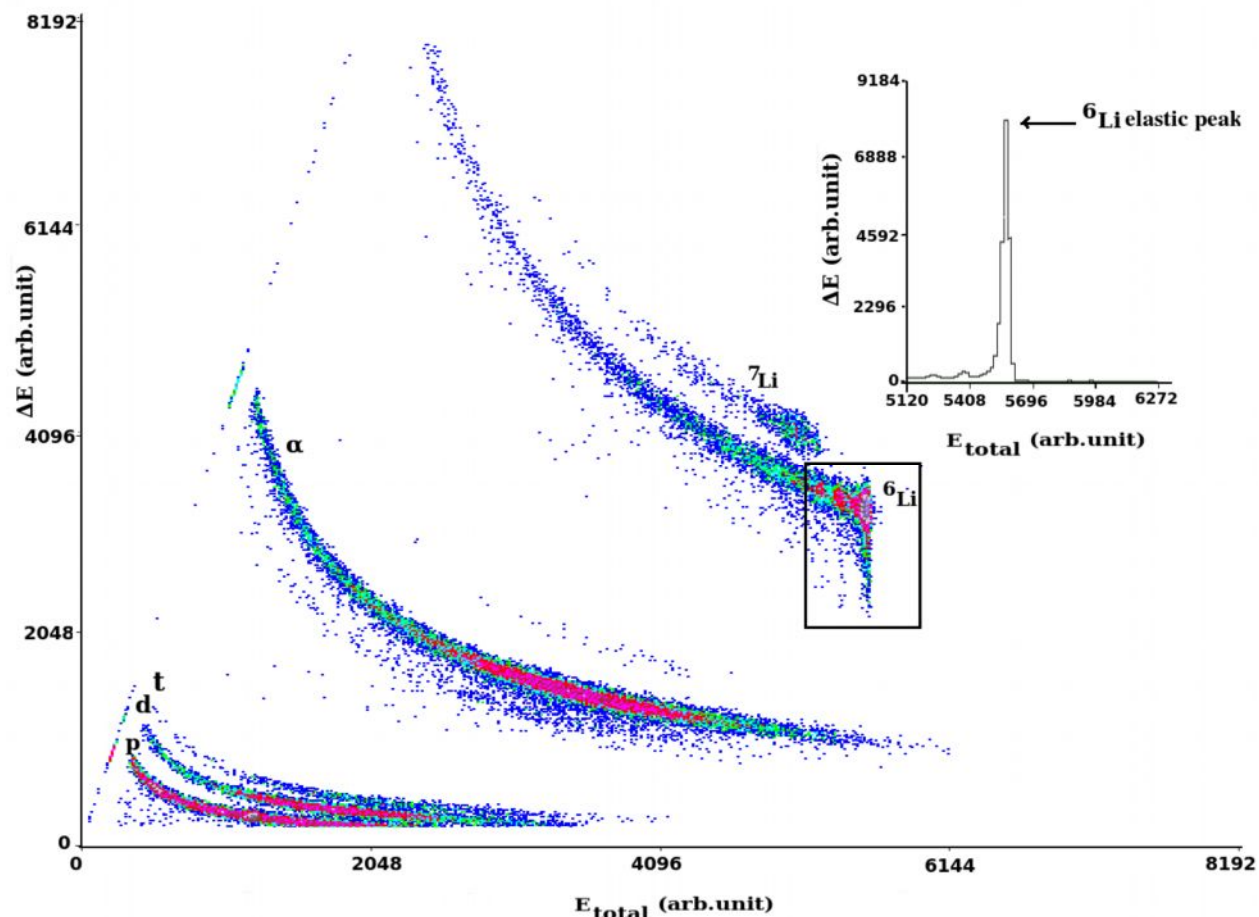


Figure 3.4 A typical bi-parametric E- $\Delta E$  spectrum for the  ${}^6\text{Li} + {}^{116}\text{Sn}$  system at  $E_{\text{lab}} = 35$  MeV and  $\theta = 35^\circ$ . The Projection of the  ${}^6\text{Li}$  elastic peak of the bi-parametric E- $\Delta E$  spectrum is shown in the inset.

### 3.4 Electronics and data acquisition

The incident radiations coming with high energy hits the target and further goes in the detector having the specific volume, and thus generates electrical signals in the output circuit. But these signals are much smaller than expected, so amplification of such signals is needed before they are processed to obtain information on the nature of the incident radiation. Thus a preamplifier is mounted close to the detector so as to satisfy the need of amplification. From preamplifier basically two outputs viz., energy and timing are further processed in various stages

to get relevant information. The schematic diagram of electronics set up for the  $\Delta E$ -E Telescopes setup which we have used for data collection is shown in the Fig. 3.5.

All analog signals from the detectors were processed using the standard NIM electronics and the data were collected using CAMAC based multiparameter data acquisition system, LAMPS [58], developed at the Bhabha Atomic Research Centre (BARC). This is very versatile and user friendly data acquisition system which allows online spectra building and the data can be saved in the ‘list mode’ on or off conditions.

## 3.5 Optical model analysis of the elastic scattering

In this section we present the analysis of the elastic scattering angular distribution data. We use two different kinds of potential, in order to check the consistency of the results that should be model independent. In section 3.5.1 we describe the analysis with a phenomenological Woods-Saxon form interaction potential and in section 3.5.2 the analysis is performed by using the double-folding Sao Paulo potential (SPP) [59,60].

### 3.5.1. Analysis Using Phenomenological Woods-Saxon Potential

The optical model fits to the elastic scattering data were performed using the ECIS code [61]. We used the real and volumetric imaginary potentials as of Woods-Saxon form. In order to avoid a fit procedure with too many parameters, we started the fit by changing only the real and imaginary depths of the potential, keeping the real and imaginary reduced radii and diffuseness as 1.06 fm and 0.67 fm, respectively. After this first fit was done, once more we kept the radii fixed and we fitted the depths of the real and imaginary potentials, but this time we varied the diffuseness from 0.49 fm to 0.57 fm, in steps of 0.02 fm. For the lowest energy it was necessary to reduce the diffuseness of the potentials to 0.43 fm to obtain physical values (attractive real nuclear potential and absorption of flux). Very good fits to the data were obtained but, as usual, we found several families of optical potential parameters that describe the angular distributions equally well. To reduce the ambiguities, we determined the radii of sensitivity  $R_{Sr}$  and  $R_{Si}$ , corresponding to the real and imaginary radii where different potentials have the same value.

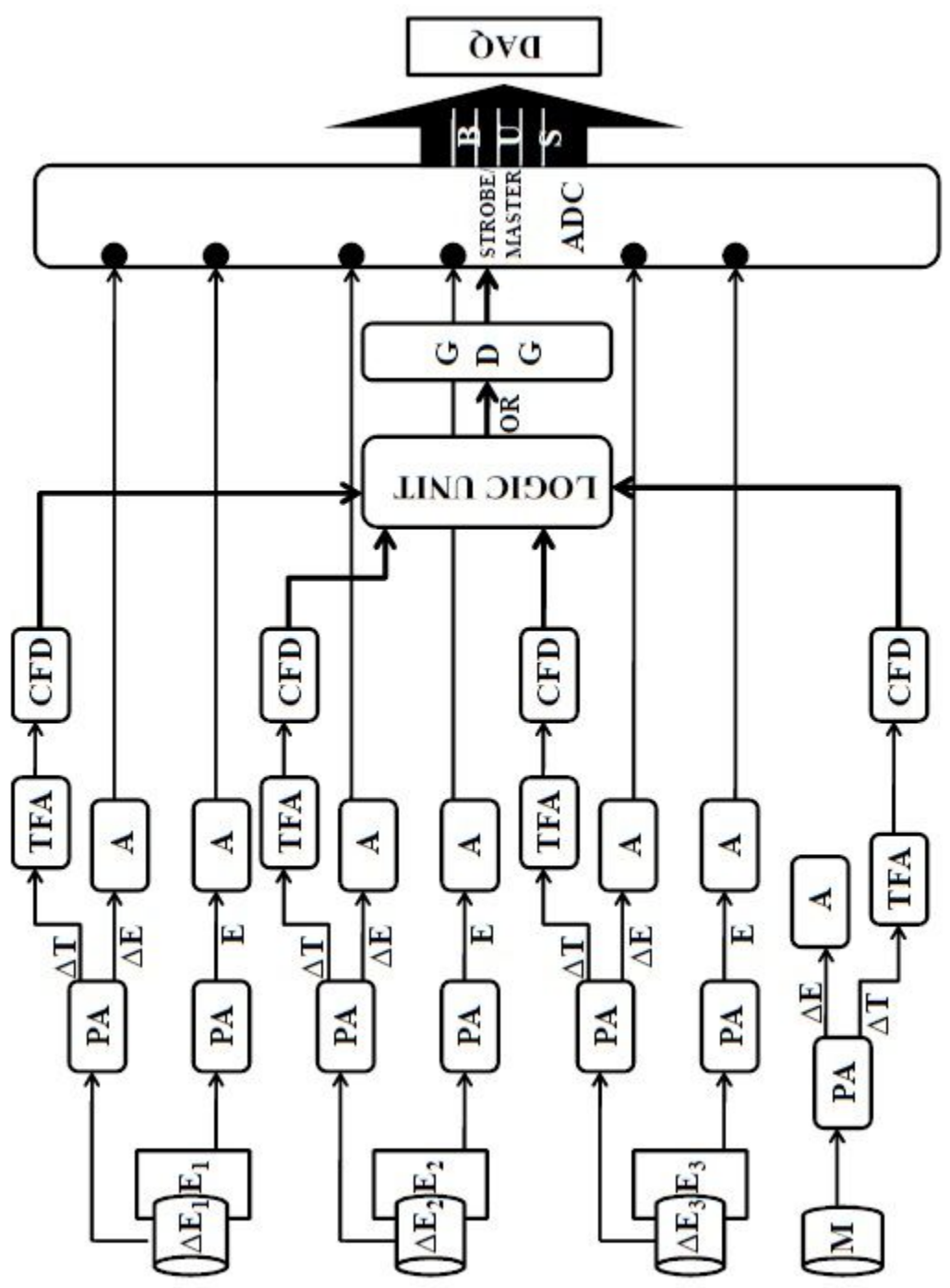


Figure 3.5 The electronics set up for the  $\Delta E$ -E telescopes used for the data collection.

- PA-Preamplifier
- A-Amplifier
- TFA-Timing Filter Amplifier
- CFD-Constant Fraction Discriminator
- G-D-G-Gate and Delay Generator
- ADC-Analog to Digital Converter
- DAQ-Data Acquisition

The derived mean sensitivity radii were 10.28 fm and 8.52 fm, respectively. Figs. 3.6 (a) and (b) show families of potentials which give similar fits, and the derivation of the real and imaginary sensitivity radii, respectively for 35 MeV. With an average sensitive radius  $R_{Sr} = 9.40$  fm (average between  $R_{Sr}$  and  $R_{Si}$ ) and the mean diffuseness  $a = 0.53$  fm for highest energies and  $a = 0.43$  fm for lowest energy, we calculated the energy dependence of the real and imaginary potentials at this radius. For  ${}^6\text{Li} + {}^{112}\text{Sn}$  system the mean diffuseness was kept to be  $a = 0.67$  fm so as to derive the total reaction cross sections. The values of  $r_v$  and  $r_i$  were kept at a fixed value of 8.37 fm each in the entire calculation. Table 3.1 shows the potential parameters which best fit the data for the  ${}^6\text{Li} + {}^{116}\text{Sn}$  system, whereas table 3.2 shows the same for the  ${}^6\text{Li} + {}^{112}\text{Sn}$  system. Figs. 3.7 – 3.8 show the experimental elastic scattering angular distributions and the best fit obtained, with the parameters shown in tables 3.1 and 3.2, respectively. One can observe that very good fits were obtained. The corresponding values of the energy dependence of the real and imaginary potentials for the  ${}^6\text{Li} + {}^{116}\text{Sn}$  system are shown in Fig. 3.9. The analysis for the search of the TA or BTA in the scattering by the  ${}^{112}\text{Sn}$  target was not possible, due to the lack of more angular distribution data. These data will be used in the next section, to derive total reaction cross sections. The error bars in Fig. 3.9 represent the range of deviation of the potential corresponding to a  $\chi^2$  variation of one unit.

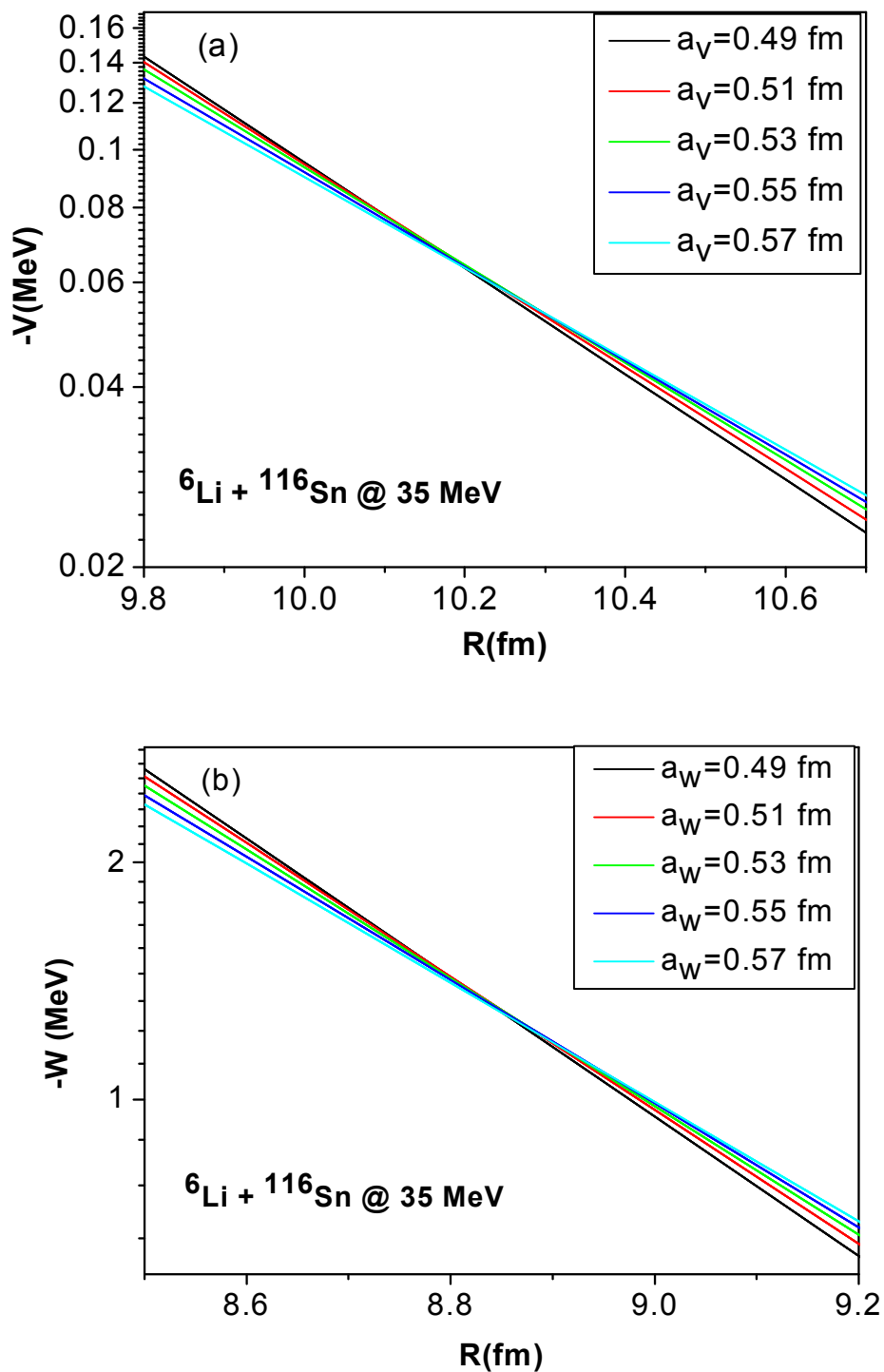


Figure 3.6 Several potentials which produce similar fits of the data, for 35 MeV. The crossing points are the derived real (a) and imaginary (b) sensitivity radii.

**Table 3.1 Parameters used with Wood-Saxon potential calculations for  ${}^6\text{Li} + {}^{116}\text{Sn}$  System and the derived total reaction cross sections.**

$E_{\text{Lab}}$ (MeV)	$a_r$ & $a_i$ (fm)	$V_r$ (MeV)	$V_i$ (MeV)	$\chi^2 / n$	$\sigma_R$ (mb)
20	0.43	222.7	2230	11.4	274
21	0.53	89	168	3.7	329
22	0.53	101	244.5	7.6	521
23	0.53	95	100	5.3	555
26	0.53	157	163	35.3	1037
30	0.53	95	68	8.7	1261
35	0.53	148	236	13.6	1826

**Table 3.2 Parameters used with Wood-Saxon potential calculations for  ${}^6\text{Li} + {}^{112}\text{Sn}$  System and the derived total reaction cross sections.**

$E_{\text{Lab}}$ (MeV)	$a_r$ & $a_i$ (fm)	$V_r$ (MeV)	$V_i$ (MeV)	$\chi^2 / n$	$\sigma_R$ (mb)
21	0.67	17	25	5.00	235
23	0.67	16	24.7	5.33	480
25	0.67	18	26	4.92	736
35	0.67	20.4	41	9.46	1660

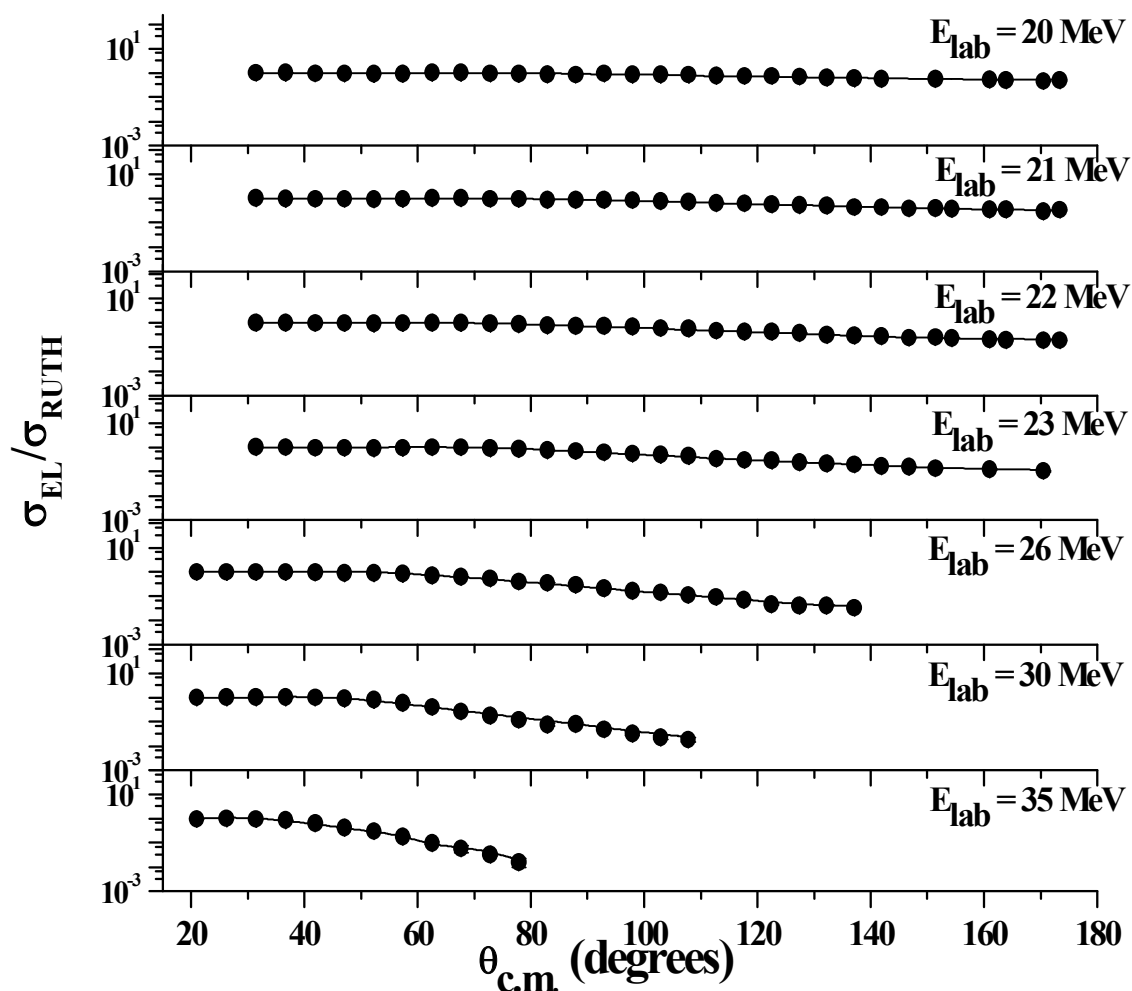


Figure 3.7 Experimental elastic scattering cross sections normalized to the Rutherford cross sections for the  ${}^6\text{Li} + {}^{116}\text{Sn}$  system and their best fits from optical model calculations. The curves correspond to best fits were obtained using the Woods-Saxon potential (WSP).

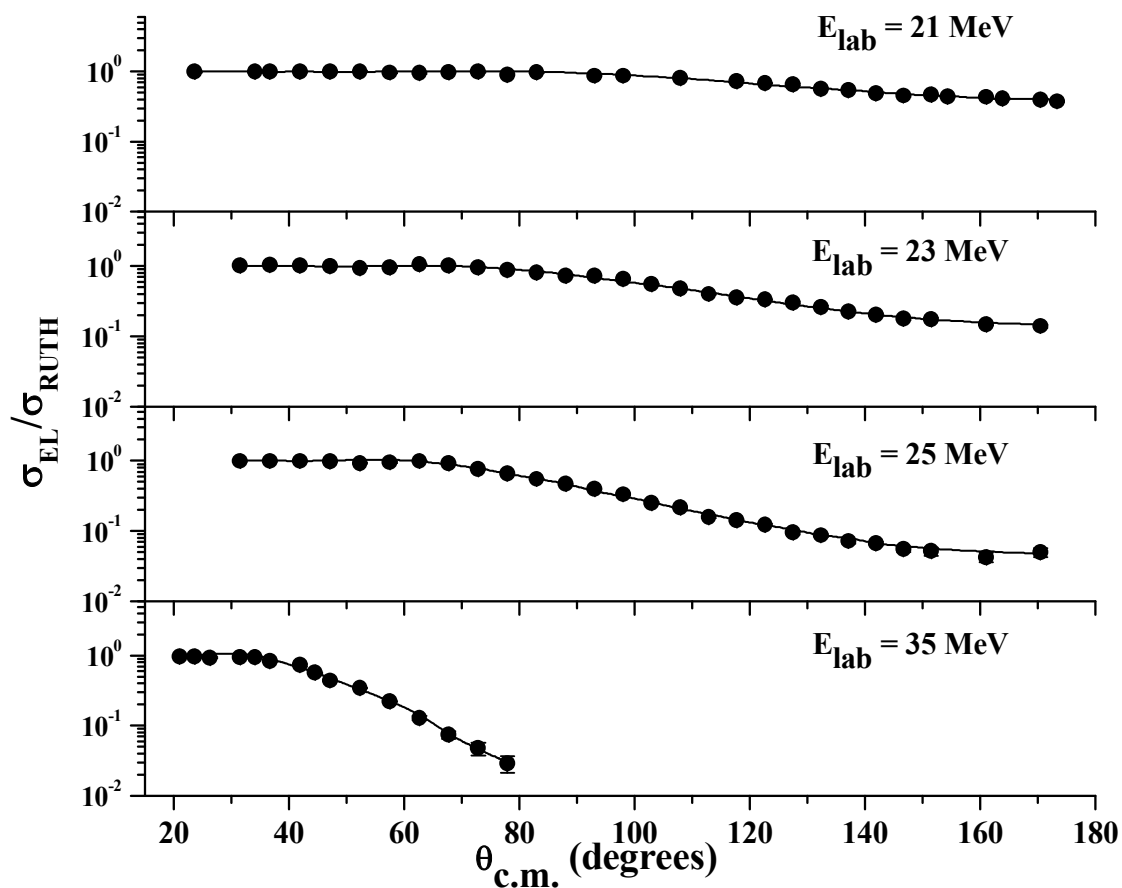
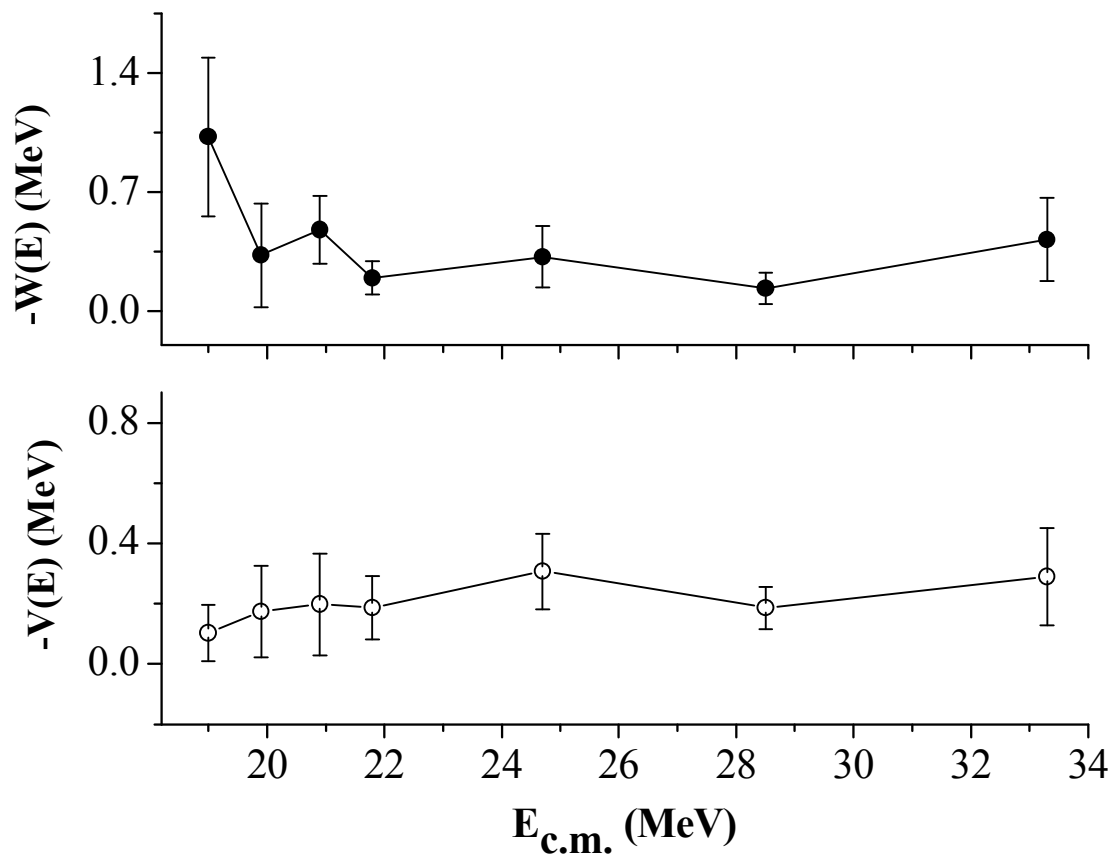


Figure 3.8 Experimental elastic scattering cross sections normalized to the Rutherford cross sections for the  ${}^6\text{Li} + {}^{112}\text{Sn}$  system and their best fits from optical model calculations. The curves correspond to best fits were obtained using the Woods-Saxon potential (WSP).



**Figure 3.9** Energy dependence of the real and imaginary parts of the optical potential obtained for the  ${}^6\text{Li}+{}^{116}\text{Sn}$  system at an average radius  $R_S=9.40$  fm. The energy  $V_b$  of the Coulomb barrier is 22.07 MeV in the centre of mass frame calculated using the Bass formula.

### 3.5.2. Analysis Using the Double-Folding Sao Paulo Potential

The Sao Paulo potential (SPP) [59,60] is an optical potential which has been successfully used to describe a large variety of systems in a wide energy range, including fusion excitation functions and barrier distributions of weakly bound nuclei [62,63]. The trivial energy dependence of the bare interaction arises from the use of a local equivalent model based on the nonlocal nature of the interaction. At a limited range of energy, as it occurs in the present work, it can be considered as usual double-folding potential based on an extensive systematization of nuclear densities extracted from elastic scattering data. The imaginary part of the interaction is assumed to have the same shape as the real part, with one single adjustable parameter  $N_I$  related to its strength. The data fit procedure is performed with only two free parameters, the normalization factors for the real and imaginary parts,  $N_R$  and  $N_I$ . The SPP has been used for the analysis of near barrier elastic scattering of weakly bound nuclei of several systems [19, 29, 30, 35 - 40, 42, 51].

The curves resulting from the best fits using the Sao Paulo potential (SPP) can hardly be distinguished from those Woods-Saxon potential and therefore were not shown in the Figs. 3.7 and 3.8. The resulting fits of the normalization parameters for the  ${}^6\text{Li} + {}^{116, 112}\text{Sn}$  system are shown in table 3.3 & 3.4. It can be observed that the energy dependence (Fig. 3.10) follows the same trend as in the previous analysis. So, our conclusions concerning the behavior of the OP energy dependence do not change when either potential is used.

**Table 3.3 Parameters used with the Sao Paulo potential calculations for  ${}^6\text{Li} + {}^{116}\text{Sn}$  System and the derived total reaction cross sections.**

$E_{\text{Lab}}$ (MeV)	$N_{\text{R}}$	$N_{\text{I}}$	$\chi^2 / n$	$\sigma_{\text{R}}$ (mb)
20	0.30	2.26	10.00	284
21	0.45	2.02	2.89	334
22	0.34	2.88	6.99	532
23	0.61	1.59	3.83	572
26	0.84	1.87	21.65	1071
30	0.83	0.95	10.44	1233
35	1.03	0.75	14.41	1599

**Table 3.4 Parameters used with the Sao Paulo potential calculations for  ${}^6\text{Li} + {}^{112}\text{Sn}$  System and the derived total reaction cross sections.**

$E_{\text{Lab}}$ (MeV)	$N_{\text{R}}$	$N_{\text{I}}$	$\chi^2 / n$	$\sigma_{\text{R}}$ (mb)
21	0.79	2.08	4.21	250
23	0.85	2.01	4.85	496
25	1.01	1.80	6.12	733
35	1.23	3.16	9.00	1691

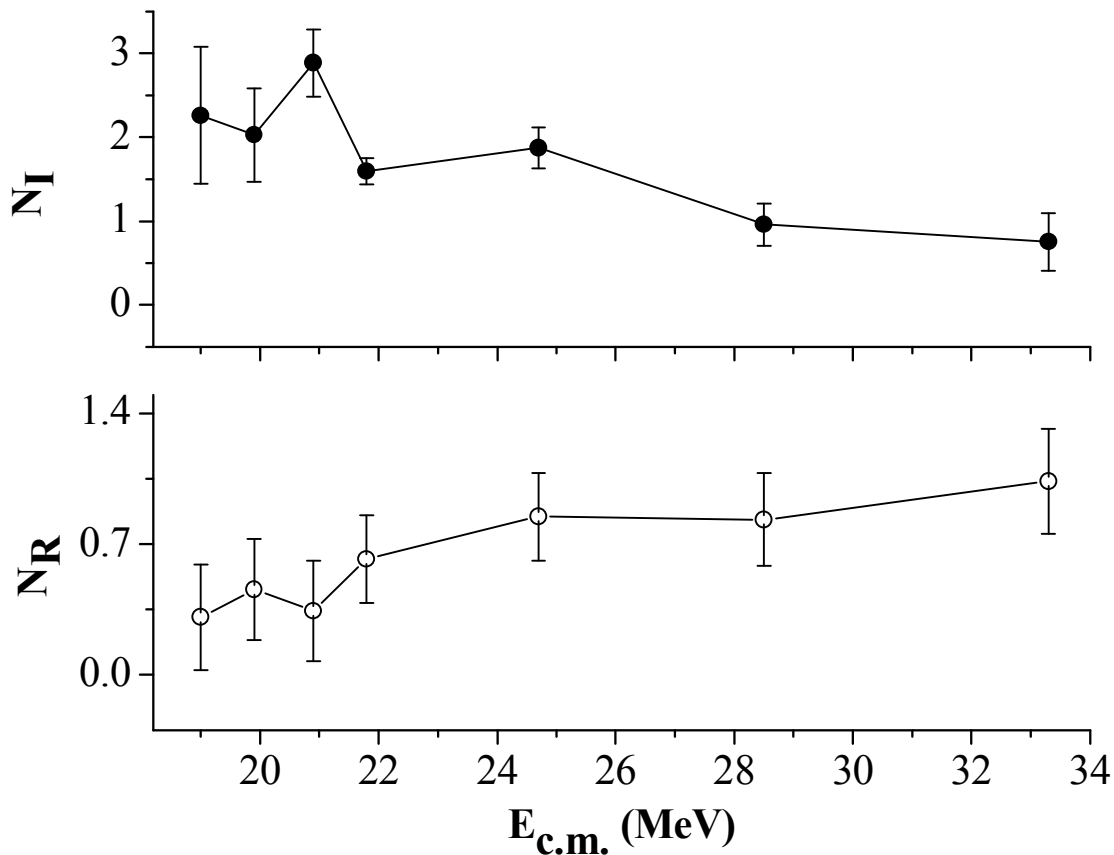


**Figure 3.10** Best fits for  $N_R$  and  $N_I$  as a function of the bombarding energy obtained from fits with the São Paulo potential for the  ${}^6\text{Li}+{}^{116}\text{Sn}$  system. The energy  $V_b$  of the Coulomb barrier is 22.07 MeV in the centre of mass frame calculated using the Bass formula.

### 3.6 Total Reaction Cross Sections for Different Systems

If one wants to perform a systematic study of excitation functions for different systems, it is required to suppress differences arising from the size and charges of the systems. Nowadays the widely used “reduction” method was proposed by Gomes et al. [64]. In this method, the quantities  $\sigma_R / (A_P^{1/3} + A_T^{1/3})^2$  versus  $E_{c.m.} / (A_P^{1/3} + A_T^{1/3})^2 / Z_P Z_T$  are plotted, where  $P$  and  $T$  are related to projectile and target, respectively, and  $\sigma_R$  is the total reaction cross section. The authors claim that this procedure removes the dependence on the masses and charges of the collision partners but not specific features of the projectile density, particularly important when weakly bound projectile nuclei are involved. However, it was recently proposed a new “reduction

method” to compare fusion cross sections of different systems [26, 27], later extended to be used with total reaction cross sections [65]. The new prescription is to plot the dimensionless quantities  $F_R(x) = (2E_{c.m.}/\hbar\omega R_B^2) \sigma_R$  versus  $x = (E_{c.m.} - V_B) / \hbar\omega$ . Here,  $V_B$ ,  $R_B$  and  $\hbar\omega$  are the height, radius and curvature parameter of the Coulomb barrier, respectively, and  $F_R(x)$  is called Total Reaction Function. Some reported works follow this new procedure [66 – 70].

In the present work we compare the total reaction cross sections derived from our experimental elastic scattering data for the  ${}^6\text{Li} + {}^{116, 112}\text{Sn}$  systems with other systems involving tightly bound, stable weakly bound and radioactive and halo projectiles with targets in the same mass range. We use both mentioned procedures. Tables 3.1, 3.2, 3.3 & 3.4 show the derived total reaction cross sections for the two systems measured in the present work.

Fig. 3.11 shows the reduced total reaction cross sections for several systems, by using the reduction prescription of Gomes et al. [64], whereas Fig. 3.12 shows the total reaction functions for the same systems, plotted as proposed by Shorto et al. [65]. The systems analyzed are:  ${}^6\text{Li} + {}^{112, 116}\text{Sn}$  [70],  ${}^4,6\text{He} + {}^{120}\text{Sn}$  [66],  ${}^8\text{Li} + {}^{120}\text{Sn}$  [67],  ${}^{6,7}\text{Li} + {}^{138}\text{Ba}$  [18],  ${}^{6,7}\text{Li} + {}^{144}\text{Sm}$  [41],  ${}^9\text{Be} + {}^{144}\text{Sm}$  [38],  ${}^{16}\text{O} + {}^{144}\text{Sm}$  [71]. The systems with the targets  ${}^{120}\text{Sn}$  and  ${}^{138}\text{Ba}$  have already been analyzed in ref [66].

From Fig. 3.11 we observe that the total reaction cross section is largest for the neutron-halo  ${}^6\text{He}$  projectile, which has very low breakup energy (0.98 MeV). Then there is the group of lithium isotope projectiles ( ${}^{6,7,8}\text{Li}$ ), with breakup threshold between 1.5 MeV and 2.5 MeV. Finally, the tightly bound projectiles  ${}^{16}\text{O}$  and  ${}^4\text{He}$  produce total reaction cross sections smaller than the weakly bound projectiles. So, we conclude that the breakup increases the total reaction cross section, and for the  ${}^6\text{He}$  nucleus, with larger breakup probability than the lithium isotopes, the cross section is even larger. This is not the same conclusion obtained for a similar analysis with the light  ${}^{27}\text{Al}$  target, for which it was found [72] that reaction cross sections induced by  ${}^6\text{He}$  is similar to the ones induced by stable weakly bound projectiles. However, for light systems, the Coulomb breakup should be much smaller than for the systems analyzed in the present work. Moreover, the transfer channels may have different influence in different mass regions. From Fig. 3.12, using an alternative reduction method, one can observe that the same conclusions can be drawn.

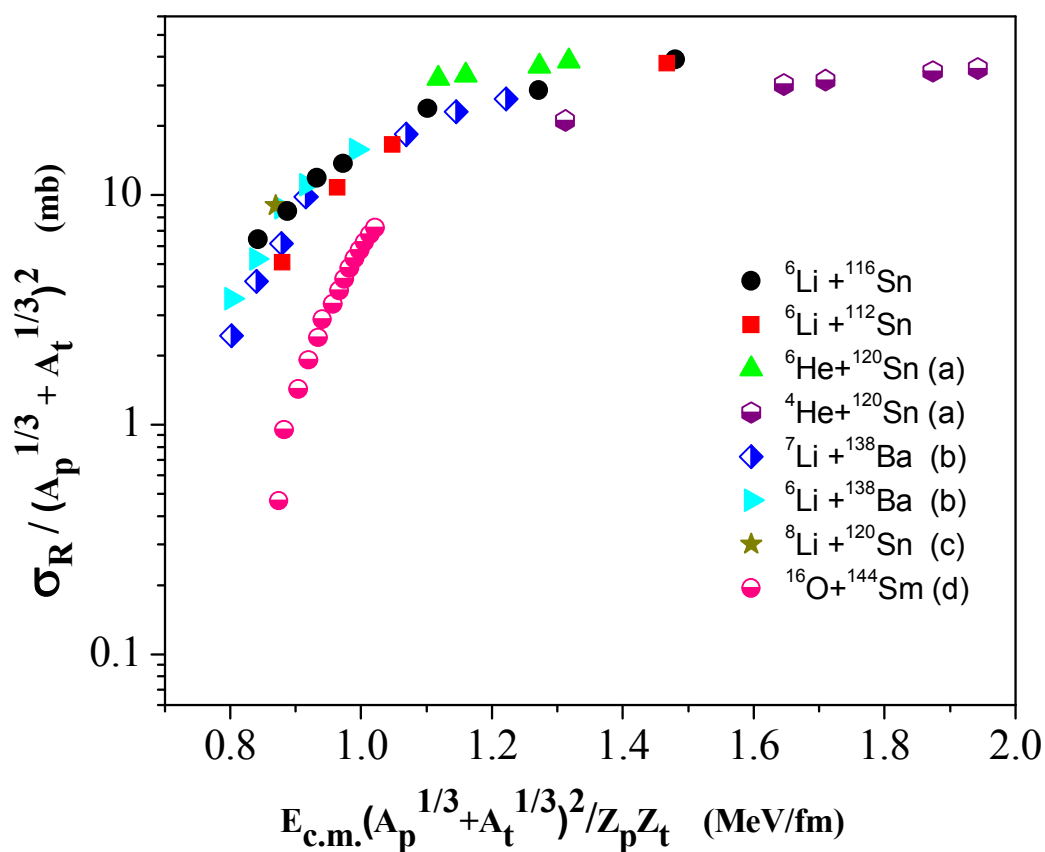


Figure 3.11 Reduced reaction cross section versus reduced projectile energy for the  $^6\text{Li} + ^{116,112}\text{Sn}$  reactions using the prescription given in Ref. [64] compared to other systems of similar masses: (a) from Ref. [66], (b) from Ref. [18], (c) from Ref. [67], (d) from Ref. [71].

The reaction cross sections were obtained from optical model fits of the experimental angular distributions.

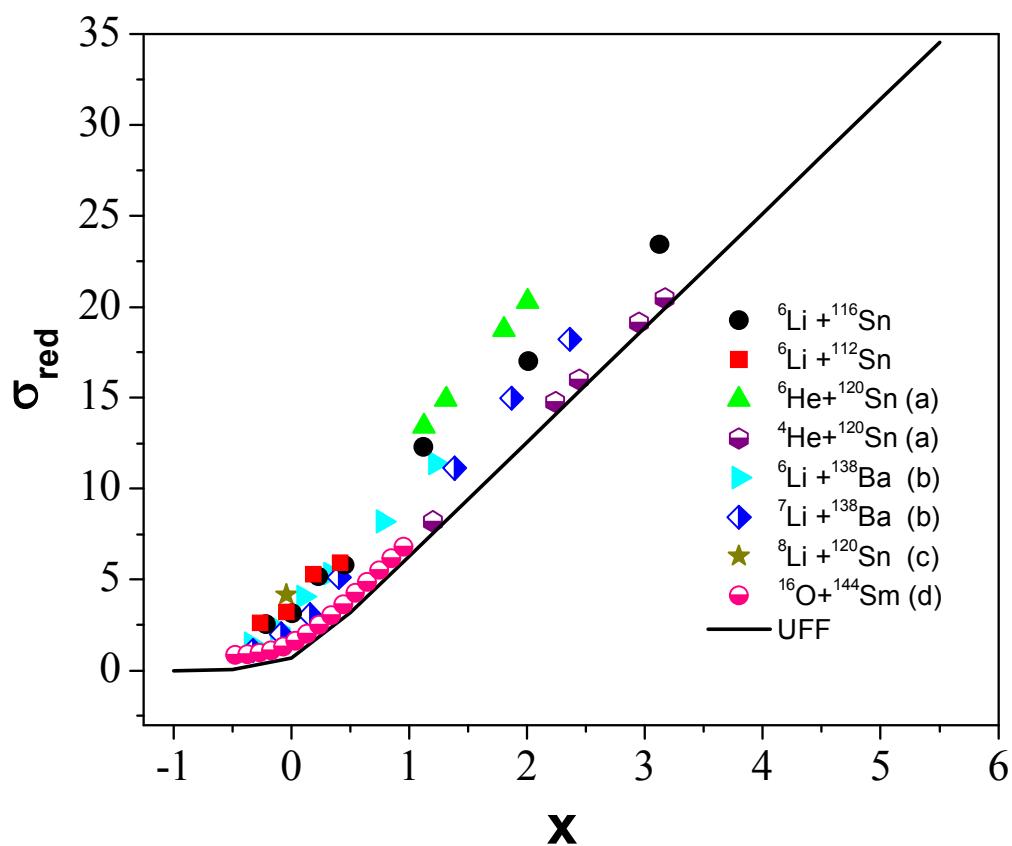


Figure 3.12 Reduced reaction cross section versus reduced projectile energy for the  ${}^6\text{Li} + {}^{116,112}\text{Sn}$  reactions using the prescription given in Ref. [65] compared to other systems of similar masses: (a) from Ref. [66], (b) from Ref. [18], (c) from Ref. [67], (d) from Ref. [71].

The reaction cross sections were obtained from optical model fits of the experimental angular distributions.

### 3.7 Effects of breakup couplings on the ${}^6\text{Li} + {}^{116}\text{Sn}$

The breakup process involves unbound states of the projectile's fragments, called the continuum states. Then, to calculate reactions involving breakup is necessary to approximate the continuum by a finite number of channels. This is achieved by continuum discretized coupled channel (CDCC) method [73]. The continuum discretized coupled channel (CDCC) method has been the best method used to study the coupling of continuum states between them and with the bound states. Scattering states are grouped to form wave packets, or bins, belonging to the Hilbert space. Non-infinite matrix elements are obtained folding the interaction potential between the bin states. We can then couple the continuum states in the same way we proceed with inelastic excitations, but with the more complex model space. The configuration space considered should be in principle infinite, but in practice it has to be truncated with the hope that the more important states were retained in the coupling scheme. Due to all these particularities, to obtain a numerical solution by means of CDCC method is not an easy task and the convergence must be checked exhaustively.

So we along with our collaborators performed the theoretical study [74] of the effect of the breakup channel on the elastic angular distributions for  ${}^6\text{Li} + {}^{116}\text{Sn}$  system using the CDCC method. The study with the  ${}^6\text{Li} + {}^{112}\text{Sn}$  system was not possible as the data was inadequate. To account for the breakup of the  ${}^6\text{Li}$  in the  ${}^6\text{Li} + {}^{116}\text{Sn}$  reaction we used a similar model space as reported in Refs. [75,76]. The  ${}^6\text{Li}$  nucleus is treated as an alpha core plus one deuteron with a separation energy of 1.47 MeV. The states of the projectile are in the continuum and are approximated by a set of square-integrable bin wave functions. The bins are linear combinations of  $\alpha + d$  scattering states, with centroids  $\varepsilon_i$  at  $\alpha - d$  relative energies in the range  $1.48 < \varepsilon_i < \varepsilon_{\text{max}}$ . We used  $\varepsilon_{\text{max}} = 7$  MeV. In this work we performed additional tests of convergence with R-matrix method.

To investigate the reaction mechanisms in  ${}^6\text{Li} + {}^{116}\text{Sn}$  scattering, we performed several coupled channel calculations, using the computer code FRESKO [77]. The transition matrix – elements were calculated for  $r_{\text{bin}} \leq 50$  fm. This was enough to guarantee the orthogonality between the bins states. The projectile - target distance in the solution of the coupled channels system was integrated numerically up to  $R_{\text{max}} = 500$  fm and relative angular momentum up to

1000  $\hbar$  were considered. The Woods-Saxon potentials used to generate the projectile's ground state  $J^\pi = 1^+$  and unbound resonant states  $3^+$ ,  $2^+$  and  $1^+$  were the same used in Refs. [75,76]. We used a double folding São Paulo Potential (SPP) [59,60] for the real part of the  $\alpha$ ,  $d + {}^{116}\text{Sn}$  optical potential. The imaginary part was an internal Woods-Saxon (WS) potential with  $W_0 = 50.0$  MeV,  $r_0 = 1.06$  fm and  $a_0 = 0.2$  fm, that guarantees the ingoing wave boundary conditions (IWBC).

For the lower energies the R-matrix method was used for the calculations of the cross section because at these energies the residual energy of the fragments is not high enough to access the higher energy bins that remain as virtual states. With S-Matrix this states are not well resolved, giving unphysical results (cross section not equal to zero). For the higher energies these states become accessible, then the calculation by means of S-matrix method is enough.

In Fig. 3.13, we compare experimental angular distributions with CDCC calculations. The blue curves represent the results of our best CDCC calculation. It includes channels corresponding to all bin states (breakup), as well as all couplings among these channels. The results are in good agreement with the data. The red curves represent the same calculation switching off the continuum-continuum couplings. The calculations are well below the experimental angular distributions for all collision energies, even at small angles. This conclusion is in agreement with the results of same CDCC calculations for  ${}^8\text{B} + {}^{58}\text{Ni}$  system [21]. In the CDCC calculations of Fig. 3.13, the entrance channel and the ones associated with the bin states of the target are coupled among themselves through the action of the potential of Eq. (3.7), that is the sum of core-target plus valence particle (triton)-target interactions,

$$V(\mathbf{R}, \mathbf{r}, \xi) = V_{cT}(\mathbf{R}, \mathbf{r}, \xi) + V_{pT}(\mathbf{R}, \mathbf{r}, \xi) \quad (3.7)$$

which contains both Coulomb and nuclear contributions. Now we investigate the relative importance of each of these contributions and the interference between them. In Fig. 3.14 the blue and the red curves represent, respectively, results of CDCC calculations considering exclusively Coulomb and nuclear breakup. We can see that for lower energies although the effect is weak, the Coulomb breakup produce attractive polarization, while the nuclear breakup produce

repulsive. For the higher energies both polarizations are irrelevant in agreement with the results of Fig. 3.13 (compare blue and black curves in Fig. 3.13).

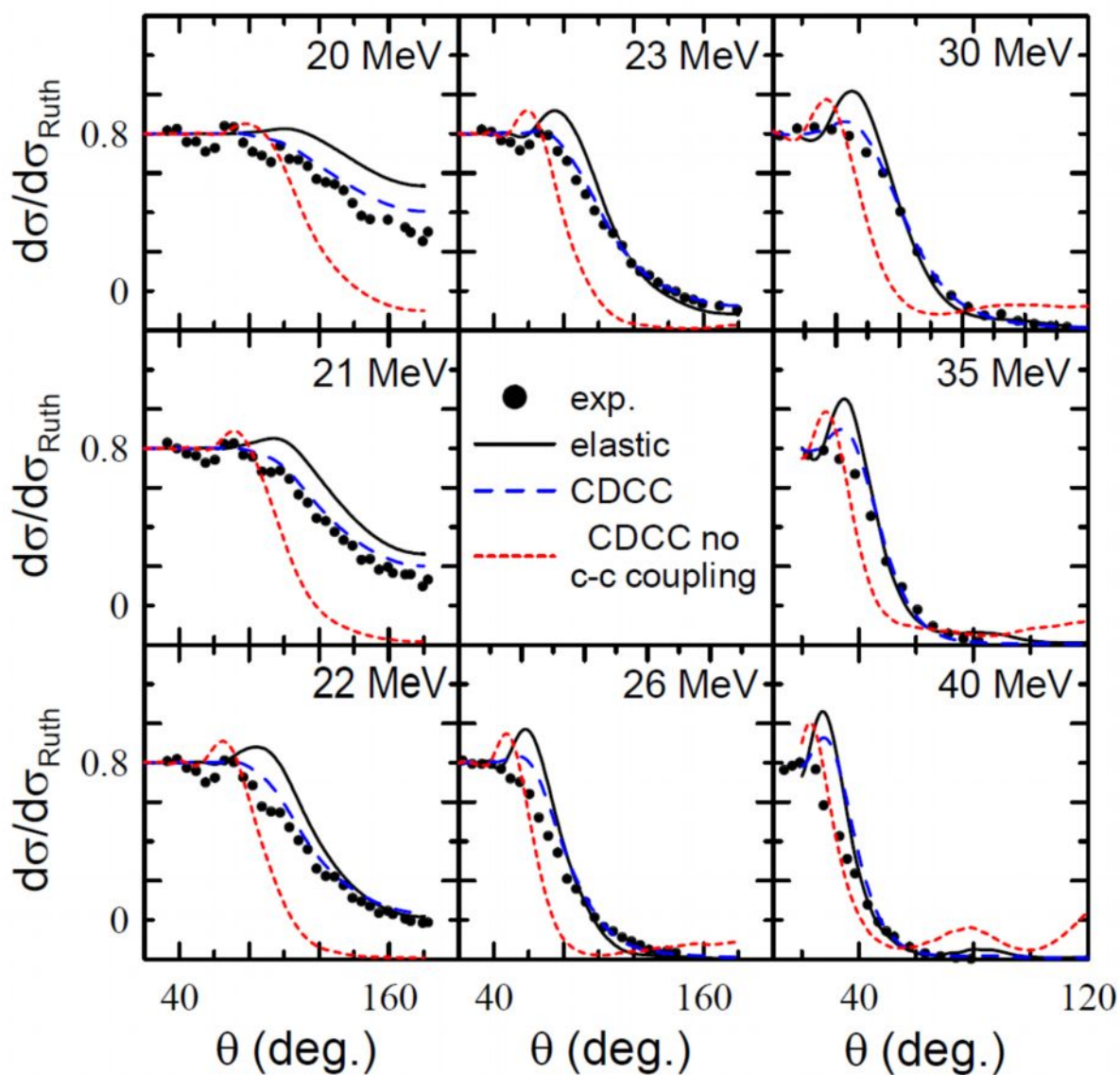


**Figure 3.13** Angular distributions predicted by CDCC calculations.

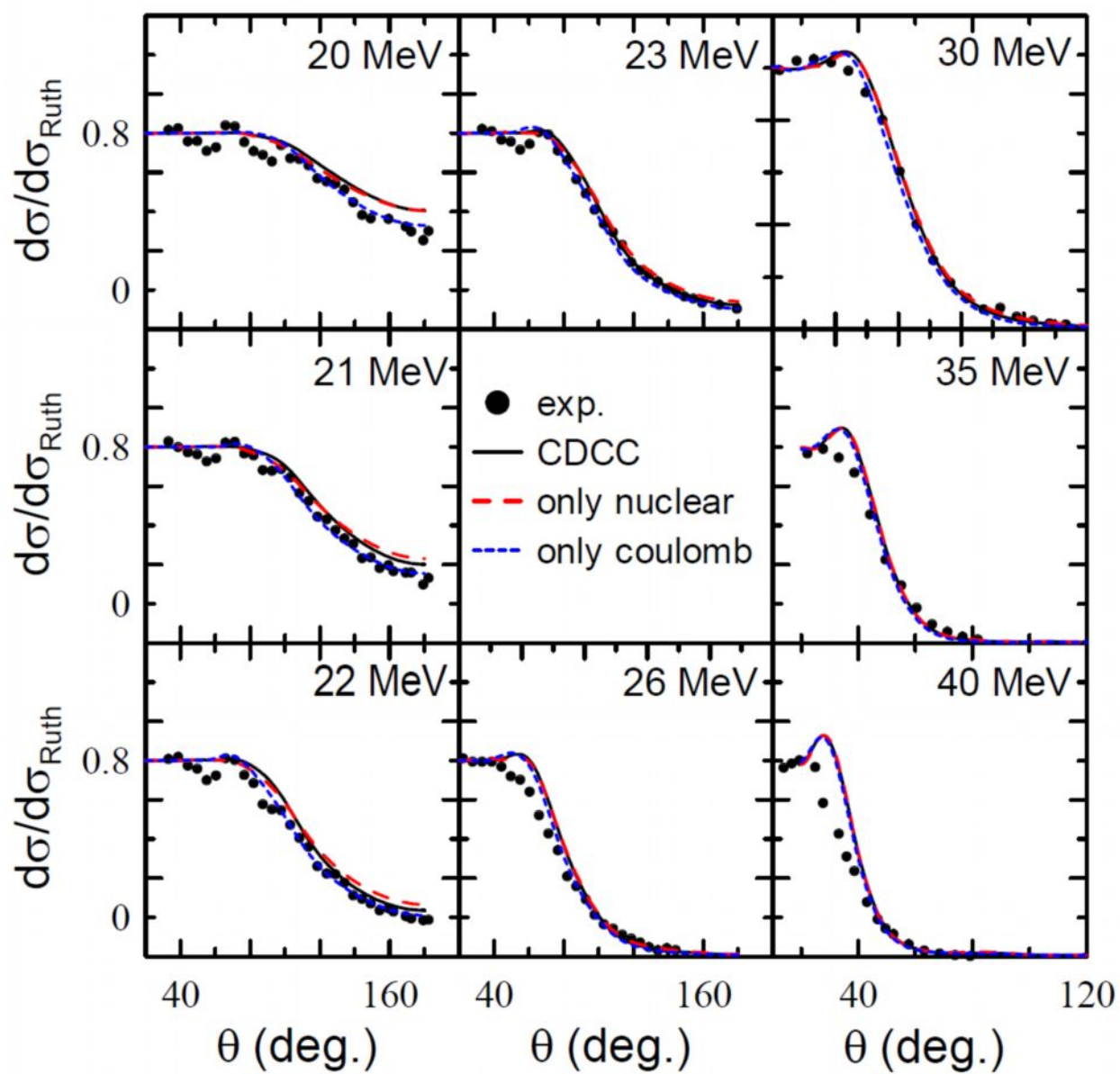
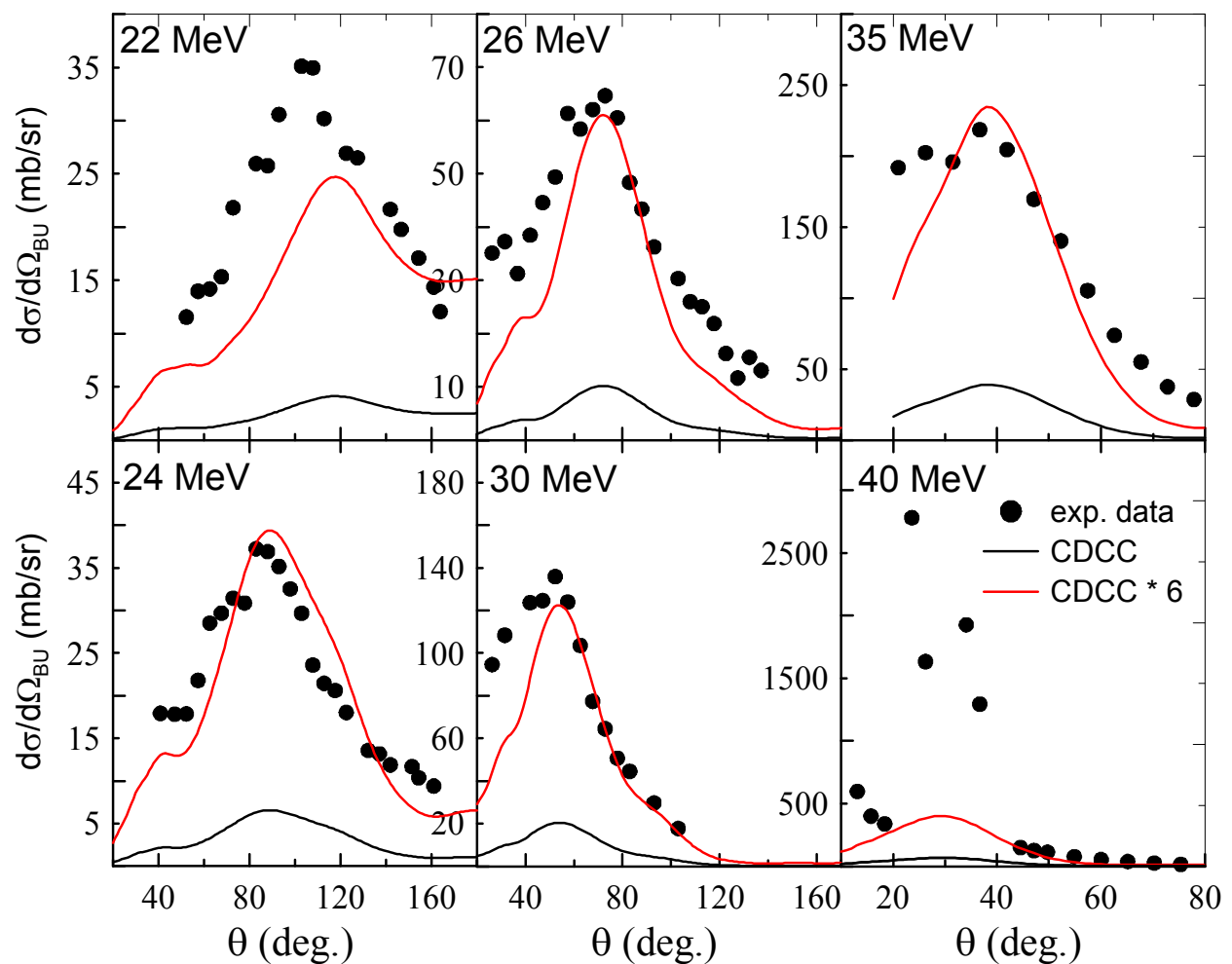


Figure 3.14 Effects of Coulomb and nuclear breakup on the elastic angular distributions.

In Fig. 3.15 it is shown a comparison between CDCC calculations of breakup cross section and experimental data (full circles). One can see that the experimental data are about one order of magnitude higher than the CDCC calculations, although the shape is quite similar. The red curve represents the CDCC calculations multiplied by an arbitrary factor of six. One can see that the agreement is good for all energies, except the higher and lower ones. This underestimation of the experimental data may be due to the fact that they are taking into account not only the alphas coming from the breakup channel, but from other reaction mechanisms, like the evaporation of complete and incomplete fusion, transfer and so on.



**Figure 3.15 Exclusive breakup cross section measured at various energies. Full circles represent experimental data and the two different lines shows CDCC calculations (see text for details).**

### 3.8 Conclusions

We have measured precise elastic scattering angular distributions, at near barrier energies, for the weakly bound  ${}^6\text{Li} + {}^{116, 112}\text{Sn}$  systems. Optical model analyzes of the energy dependence of the interaction potential, performed by two different kinds of potentials, show the absence of the usual Threshold Anomaly (TA), corresponding to the presence of the so-called breakup Threshold Anomaly (BTA). This behavior is attributed to the repulsive polarization potential produced by the breakup process. The analysis of total reaction cross sections for several systems with similar target masses indicates that the breakup increases the total reaction cross section in such way that the neutron-halo  ${}^6\text{He}$  projectile induced reactions have larger cross section than the not so weakly bound lithium isotopes, which, however, have larger cross sections than the tightly bound projectiles investigated. Also we have measured near-barrier  $\alpha$  – production cross sections for the weakly bound nucleus  ${}^6\text{Li}$  on  ${}^{116}\text{Sn}$ . CDCC calculations have been performed considering the exclusive Coulomb and nuclear breakup along with the Exclusive breakup cross section measured at various energies which clearly indicates alphas coming from the breakup channel along with the other reaction mechanisms, like the evaporation of complete and incomplete fusion, transfer and so on.

## References

- [1] M.A. Nagarajan, C.C. Mahaux, G.R. Satchler, Phys. Rev. Lett. **54**, 1136 (1985)
- [2] G.R. Satchler, Phys. Rep. **199**, 147 (1991)
- [3] M.E. Brandan, G.R. Satchler, Phys. Rep. **285**, 143 (1997)
- [4] C. Mahaux, H. Ngo, G.R. Satchler, Nucl. Phys. A **449**, 354 (1986)
- [5] G.R. Satchler, W. Love, Phys. Rep. **55**, 183 (1979)
- [6] L.F. Canto, P.R.S. Gomes, R. Donangelo, M.S. Hussein, Phys. Rep. **424**, 1 (2006)
- [7] D.J. Hinde *et al.*, Phys. Rev. Lett. **89**, 272701 (2002)
- [8] E.F. Aguilera *et al.*, Phys. Rev. Lett. **84**, 5058 (2000);
- [9] E.F. Aguilera *et al.*, Phys. Rev. C **63**, 061603 (R) (2001)
- [10] C. Signorini, Eur. Phys. J A **13**, 129 (2002)
- [11] C. Signorini *et al.*, Phys. Rev. C **67**, 044607 (2003)
- [12] Y.W. Wu *et al.*, Phys. Rev. C. **68**, 044605 (2003)
- [13] A. Pakou *et al.*, Phys. Lett. B **556**, 21 (2003);
- [14] A. Pakou *et al.*, Phys. Rev. C **69**, 054602 (2004);
- [15] A. Pakou *et al.*, Phys. Rev. C **78**, 067601 (2008)
- [16] P.R.S. Gomes *et al.*, Phys. Lett. B **634**, 356 (2006)
- [17] N. Keeley *et al.*, Nucl. Phys. A **571**, 326 (1994)
- [18] A.M.M. Maciel *et al.*, Phys. Rev. C **59**, 2103 (1999)
- [19] J. Lubian *et al.*, Nucl. Phys. A **791**, 24 (2007)
- [20] J. Lubian *et al.*, Phys. Rev. C **78**, 064615 (2008)
- [21] J. Lubian *et al.*, Phys. Rev. C **79**, 064605 (2009)
- [22] Y. Sakuragi, M. Yahiro, M. kamimura, Prog. Theor. Phys. **70**, 1047 (1983)
- [23] N. Keeley, K. Rusek, Phys. Lett. B **427**, 1 (1998)
- [24] N. Keeley, K.W. Kemper, K. Rusek, Phys. rev. C **66**, 044605 (2002)
- [25] V.N. Garcia *et al.*, Phys. Rev. C **80**, 037602 (2009)
- [26] L.F. Canto *et al.*, J. Phys. G **36**, 015109 (2009)
- [27] L.F. Canto *et al.*, Nucl. Phys. A **821**, 51 (2009)
- [28] P.R.S. Gomes, J. Lubian, L.F. Canto, Phys. Rev. C **79**, 027606 (2009)
- [29] M.S. Hussein *et al.*, Phys. Rev. C **73**, 044610 (2006)

- [30] P.R.S. Gomes *et al.*, J. Phys. G **31**, S1669 (2005)
- [31] S.B. Moraes *et al.*, Phys. Rev. C **61**, 064608 (2000)
- [32] J. Lubian *et al.*, Phys. Rev. C **64**, 027601 (2001)
- [33] R.J. Woolliscroft *et al.*, Phys. Rev. C **69**, 044612 (2004)
- [34] I. Martel *et al.*, Nucl. Phys. A **605**, 417 (1996)
- [35] P.R.S. Gomes *et al.*, Phys. Rev. C **70**, 054605 (2004)
- [36] P.R.S. Gomes *et al.*, Phys. Rev. C **71**, 034608 (2005)
- [37] P.R.S. Gomes *et al.*, Phys. Rev. C **73**, 064606 (2006)
- [38] P.R.S. Gomes *et al.*, Nucl. Phys. A **828**, 233 (2009)
- [39] J.M. Figueira *et al.*, Phys. Rev. C **73**, 054603 (2006);
- [40] J.M. Figueira *et al.*, Phys. Rev. C **75**, 017602 (2007)
- [41] J.M. Figueira *et al.*, Phys. Rev. C **81**, 024613 (2010)
- [42] J.O. Fernandez Niello *et al.*, Nucl. Phys. A **787**, 484c (2007)
- [43] A. Gomez Camacho *et al.*, Phys. Rev. C **76**, 044609 (2007)
- [44] A. Gomez Camacho *et al.*, Phys. Rev. C **77**, 054606 (2008)
- [45] H. Kumawat *et al.*, Phys. Rec. C **78**, 044617 (2008)
- [46] C. Signorini *et al.*, Phys. Rev. C **61**, 061603 (R) (2000);
- [47] M. Zadro *et al.*, Phys. Rev. C **80**, 064610 (2009)
- [48] M. Biswas *et al.*, Nucl. Phys. A **802**, 67 (2008)
- [49] E.F. Aguilera *et al.*, Phys. Rev. C **79**, 021601 (R) (2009)
- [50] A.R. Garcia *et al.*, Phys. Rev. C **76**, 067603 (2007)
- [51] A. Gomez Camacho *et al.*, Nucl. Phys. A **833**, 156 (2010)
- [52] K.G. Prasad Nucl. Instrum. Meth. B **40/41**, 916 (1989).
- [53] S. S. Kapoor *et al.*, Indian Jour. of Pure and Applied Phys. **27**, 623 (1989).
- [54] A. Navin, M. Dasgupta, C. V. K. Baba, and A. Roy, in proceedings of DAE symposium on Nuclear Physics, vol. B **32**, p. 59 (1989).
- [55] S. A. Kori *et al.*, Int. Conf. on Data Acquisition and Control of Accelerators, VECC, Calcutta, 155 (1991).
- [56] J. Ziegler, [www.srim.org](http://www.srim.org)
- [57] M.S. Livingston, H.A. Bethe Rev. Mod. Phys. **9**:261, (1937).

- [58] A. Chatterjee, LAMPS: Linux Advanced Multiparameter System (2008), <http://www.tifr.res.in/pell/lamps.html>
- [59] L.C. Chamon *et al.*, Phys. Rev. Lett. **79**, 5218(1997).
- [60] L.C. Chamon *et al.*, Phys. Rev. C **66**, 014610 (2002).
- [61] J. Raynal, Phys. Rev. C **23**, 2571 (1981).
- [62] E. Crema, L.C. Chamon, P.R.S. Gomes, Phys. Rev. C **72**, 034610 (2005).
- [63] E. Crema, P.R.S. Gomes, L.C. Chamon, Phys. Rev. C **75**, 037601 (2007).
- [64] P.R.S. Gomes *et al.*, Phys. Rev. C **71**, 017601 (2005).
- [65] J.M. B. Shorto *et al.*, Phys. Lett. B **678**, 77 (2009).
- [66] P.N. de Faria *et al.*, Phys. Rev. C **81**, 044605 (2010).
- [67] P.N. de Faria, Ph.D. thesis, IFUSP, 2009.
- [68] S. Mukherjee *et al.*, Europ. Phys. J A **45**, 23 (2010).
- [69] A. Lemasson *et al.*, Phys. Rev. Lett. **103**, 232701 (2009).
- [70] N. N. Deshmukh *et al.*, Phys. Rev. C **83**, 024607 (2011).
- [71] J. R. Leigh *et al.*, Phys. Rev. C **52**, 3151 (1995).
- [72] E.A. Benjamim *et al.*, Phys. Lett. B **647**, 30 (2007).
- [73] Y. Sakuragi, M. Yahiro, and M. Kamimura, Prog. Theor. Suppl. **89**, 136 (1986).
- [74] T. Correa, J. Lubian, P.R.S. Gomes, V. Guimarães, N. N. Deshmukh, and S. Mukherjee, Meeting of Physics 2011, ID: 1126-1 [2.BRNU], June 5 – 10, 2011, Rafain Hotel and Convention centre, Foz do Iguaçu, Brazil.
- [75] A. Diaz-Torres, I.J. Thompson, C. Beck, Phys. Rev. C **68**, 044607 (2003).
- [76] D.R. Otomar *et al.*, Phys. Rev. C **80**, 034614 (2009).
- [77] I. J. Thompson, Comput. Phys. Rep. **7**, 167 (1988).